Chemical Science

ROYAL SOCIETY OF CHEMISTRY

EDGE ARTICLE

View Article Online
View Journal | View Issue

Cite this: *Chem. Sci.*, 2025, **16**, 9424

All publication charges for this article have been paid for by the Royal Society of Chemistry

A mechanism-guided descriptor for the hydrogen evolution reaction in 2D ordered double transition-metal carbide MXenes†

Junmei Du, Yifan Yan, Xiumei Li, Jiao Chen, Chunsheng Guo, Yuanzheng Chen * and Hongyan Wang *

Received 26th December 2024
Accepted 21st April 2025

DOI: 10.1039/d4sc08725a

rsc.li/chemical-science

Selecting effective catalysts for the hydrogen evolution reaction (HER) among MXenes remains a complex challenge. While machine learning (ML) paired with density functional theory (DFT) can streamline this search, issues with training data quality, model accuracy, and descriptor selection limit its effectiveness. These hurdles often arise from an incomplete understanding of the catalytic mechanisms. Here, we introduce a mechanism-guided descriptor (δ) for the HER, designed to enhance catalyst screening among ordered transition metal carbide MXenes. This descriptor integrates structural and energetic characteristics, derived from an in-depth analysis of orbital interactions and the relationship between Gibbs free energy of hydrogen adsorption (ΔG_H) and structural features. The proposed model ($\Delta G_H = -0.49\delta - 2.18$) not only clarifies structure–activity links but also supports efficient, resource-effective identification of promising catalysts. Our approach offers a new framework for developing descriptors and advancing catalyst screening.

1. Introduction

Hydrogen generated through clean and sustainable methods is vital for transitioning away from carbon-based fuels to renewable energy.[1–3] Although noble metals such as platinum (Pt) are effective catalysts for the hydrogen evolution reaction (HER), their scarcity and high cost limit large-scale applications.[4,5] Thus, developing cost-effective electrocatalysts with high efficiency and low overpotential is essential, highlighting the need for non-precious alternatives.[6–9]

This study focuses on 2D ordered double transition-metal carbide (DTM) MXenes, derived from 312 and 413 MAX phases, respectively, which show strong potential for electrocatalytic water splitting due to their tunable structures and properties.[10,11] By incorporating distinct transition metals and various surface functional groups, these MXenes offer a broad range of candidates for HER catalysis, necessitating efficient screening methods to identify optimal combinations.[12]

To date, most researchers have relied on high-throughput density functional theory (DFT) calculations to evaluate the HER performance of these MXenes.[13–17] Although DFT provides accurate results, its computational expense limits its scalability for large datasets. This dilemma has evoked increasing interest in developing simpler descriptors that correlate with HER performance, allowing for more efficient predictions.[18] Several structural and electronic descriptors have been proposed, including metal–oxygen bond strength in the outer layer of MXenes,[15] which is closely related to HER activity, and the d-band center has also been shown to provide some insight into HER performance.[11] Other descriptors, such as oxygen vacancy formation energy (E_f), have also been suggested, although they are supported by data from only a limited number of DTM MXenes.[19]

Machine learning (ML)-based approaches have also been explored.[20,21] For example, B. Abraham *et al.* applied the Gradient Boosting Regressor (GBR) algorithm to predict G_H of MM′XT$_2$-type MXenes with a low mean absolute error (MAE) and high coefficient of determination (R^2) of 0.358 eV and 0.826, respectively.[22] Besides, interpretable ML models are built based on the GBR with recursive feature elimination (RFE), hyperparameter optimization (HO) and the leave-one-out (LOO) approach to identify the number of valence electrons (V_T), electron affinity (E_{AT}) of the terminating groups and d-band center variance with respect to the average (dbc_σ^2) as the strong key predictors of the Gibbs free energy. Anand *et al.* proposed the descriptor $d_{av} \times \chi_{M'}$ for DTM MXenes, which combines the average distance of the seven nearest neighbors (d_{av}) to the active site and the electronegativity of the outer-layer metal ($\chi_{M'}$).[11] Although ML methods such as the Symbolic Regression-Sure Independence Screening and Sparsifying Operator (SISSO) can generate reliable descriptors and exact relationships between descriptors and catalytic activity, they

School of Physical Science and Technology, Key Laboratory of Advanced Technology of Materials, Southwest Jiaotong University, Chengdu, Sichuan 610031, China. E-mail: hongyanw@swjtu.edu.cn; cyz@swjtu.edu.cn

† Electronic supplementary information (ESI) available. See DOI: https://doi.org/10.1039/d4sc08725a

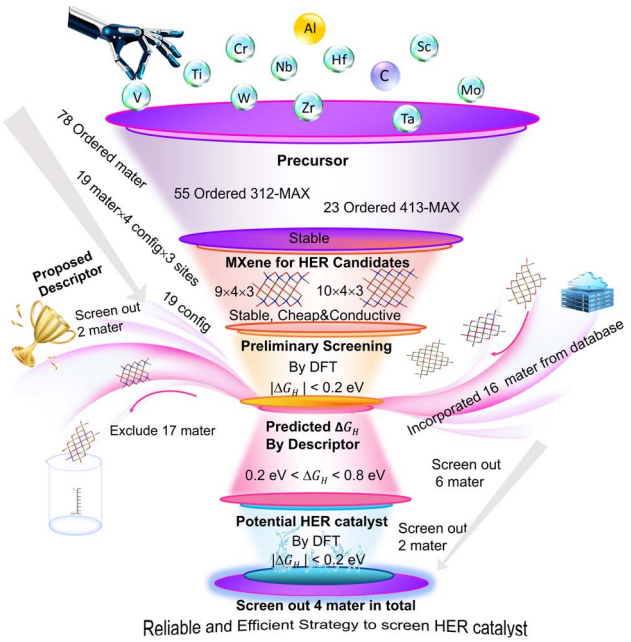

Fig. 1 A reliable and efficient flow diagram for screening ideal HER catalysts among ordered double transition-metal carbide MXenes. 'Config' denotes configuration, and 'Mater' denotes material.

primarily identify mathematical patterns rather than providing a deep mechanistic understanding of catalytic activity. This focus on statistical relationships limits their ability to predict HER activity from the necessary physical and chemical insights. Besides, ML relies on large, high-quality datasets and careful descriptor selection as well as a proper optimization algorithm. Considering these challenges, it is crucial to accurately predict HER activity and gain a more comprehensive understanding from the physical/chemical insights of the structure–activity relation simultaneously.

In this study, we propose a reliable strategy to explore ordered DTM MXenes as promising non-precious HER catalysts, as illustrated in Fig. 1. We first evaluate the synthesizability, stability, and conductivity of MXenes. Then, the promising candidates for the HER are identified by using DFT. Subsequently, their structure–catalytic activity relationships are analyzed based on both microscopic and macroscopic perspectives, and a correlative descriptor (δ) is developed based on it for deeper insights. Finally, the descriptor is validated as a reliable and efficient tool for screening additional potential MXene catalysts. Consequently, we proposed a mechanism-guided universal screening descriptor for the HER based on ordered DTM MXenes.

2. Computational details

2.1. DFT calculations

The Vienna *Ab initio* Simulation Package (VASP) code[23] was utilized based on spin-polarized DFT. The Perdew–Burke–Ernzerhof (PBE) functional within the generalized gradient approximation (GGA) was applied to model exchange–correlation interactions,[24] and the projector augmented wave (PAW)[25] method was used for core and valence electron interactions. For valence electrons, configurations included Ti [$3d^3 4s^1$], V[$3p^6 3d^4 4s^1$], Cr[$3d^5 4s^1$], Zr[$4s^1 4p^1 5s^1 4d^1$], Nb [$4p^1 5s^1 4d^1$], Mo[$4p^1 5s^1 4d^1$], Hf[$5p^1 6s^1 5d^1$], Ta[$5p^1 6s^1 5d^1$], W [$5p^1 6s^1 5d^1$], O[$2s^2 2p^4$], C[$2s^2 2p^2$], and H[$1s^1$]. A kinetic energy cut-off of 500 eV was used, with convergence criteria of 1×10^{-5} eV for energy and 0.01 eV Å^{-1} for force. The Monkhorst–Pack scheme was employed to sample the Brillouin zone with *k*-point meshes of $11 \times 11 \times 1$ for unit cells and $5 \times 5 \times 1$ for $2 \times 2 \times 1$ supercells. Detailed information of the coverage test of the *k*-point mesh and energy cutoff for accuracy is provided in Fig. S1.† A 20 Å vacuum along the *z*-direction minimized layer interactions, and Grimme's DFT + D3 was employed for van der Waals corrections.[26,27] Dipole corrections and standard conditions ($U = 0$, pH = 0, $p = 1$ bar, and $T = 298$ K) were applied. Implicit solvation using the GLSSA13 solvent model[28] was implemented *via* the VASPsol extension.[29,30] The pCOHP analysis was performed using the LOBSTER 4.1.0 package.[31,32]

2.2. Gibbs free energy of hydrogen adsorption

The overall HER pathway consists of two reaction steps, which can be summarized as follows:

$$H^+(aq) + e^- + * \rightarrow H^* \rightarrow 1/2H_2(g)\ \Delta G^0 = 0\ \text{eV} \quad (1)$$

The Volmer reaction begins with an adsorbed state involving a proton (H^+) in aqueous solution, an electron (e^-), and pristine MXene at an active site. The adsorbed hydrogen forms an intermediate (H*). The subsequent desorption of hydrogen yields hydrogen gas (H_2). The Gibbs free energy (ΔG) of the intermediate hydrogen adsorption is critical for evaluating the catalyst's hydrogen evolution reaction (HER) activity. According to the Sabatier principle, optimal HER catalysts have ΔG close to zero, as shown in the computational hydrogen electrode model (CHEM) by Nørskov *et al.*,[33,34] under standard conditions ($U = 0$, pH = 0, $p = 1$ bar, and $T = 298.15$ K), which can be expressed as:

$$\Delta G_H = \Delta E_H + \Delta E_{ZPE} + \Delta U_{0T} - T\Delta S \quad (2)$$

where ΔE_H is the adsorption energy of the intermediate species in the hydrogen evolution reaction, which is obtained from

$$\Delta E_H = \Delta E_{H^*} - \Delta E_* - \frac{1}{2}E_{H_2} \quad (3)$$

where E_{H^*}, E^*, and E_{H_2} are the total energy of the MXene with one adsorbed H atom, the energy of the pristine MXene without an adsorbed H atom, and the total energy of H_2 in the gas phase, respectively. These energies are obtained from first-principles calculations. ΔE_{ZPE} in eqn (2) is the zero-point energy between atomic hydrogen adsorption and hydrogen in the gas phase, which can be calculated using

$$\Delta E_{ZPE} = E_{ZPE}^{H^*} + \Delta E_{ZPE}^{*} - \frac{1}{2}E_{ZPE}^{H_2} \quad (4)$$

where $\Delta U_0 \rightarrow T$ and ΔS are the difference in internal energy from 0 K to T K and the entropy change, respectively. These

thermodynamic energy correction values are obtained from calculations with the aid of VASPKIT, which is the VASP post-processing code.[35]

3. Results and discussion

3.1. Constructing ordered double transition metal carbide O-terminated MXenes

This study examines synthesizable ordered DTM MXenes, specifically M′2M″C2T2 and M′2M″$_2$C$_3$T$_2$, derived from the 312 and 413 MAX phases, respectively.[10] The 312 MAX phase has a metal-to-carbon composition ratio of M′ : M″ : M : C as 2 : 1 : 1 : 2, while the 413 MAX phase follows a 2 : 2 : 1 : 3 ratio. We evaluate the synthesis, stability, and conductivity of these MXenes.

Synthesis potential is assessed by identifying stable precursor MAX phases, with formation energies below 20 eV per atom at 0 K considered stable (details in Table S1†).[36] Among 55 chemically ordered 312 MAX phases, nine are stable, while ten stable structures are found among 23 413 phases. These results align with findings by Martin Dahlqvist *et al.*, who noted similar stability trends under typical synthesis conditions ($\Delta H_{cp} < 0$ or $0 \leq \Delta H_{cp} \leq 50$ at 1773 K).[37] To enhance synthesis feasibility and cost-effectiveness, we excluded phases containing rare or expensive elements, such as Sc. Ultimately, 19 stable MAX phases are identified as viable precursors for M′2M″C$_2$T$_2$ and M′$_2$M″$_2$C$_3$T$_2$ MXenes, which will be explored for their potential in HER applications.

Specifically, under practical HER conditions, characterizing electrocatalyst surface structures is essential for screening high-performance candidates.[38–41] The surfaces of bare MXenes fully terminated by O* or OH* functional groups under the relevant U_{SHE} and pH values are investigated by calculating their Pourbaix diagrams, as shown in Fig. 2. The results indicate that fully O*-terminated surfaces are the most thermodynamically stable for Cr_2TiC_2. In contrast, for other MXenes, mixed OH*/O* terminations are more stable under acidic conditions, whereas full O*-termination becomes increasingly favorable as the pH increases. These trends are consistent with prior theoretical and experimental reports.[42,43] Based on these insights, we focus our subsequent HER analysis on the O*-terminated MXene surfaces. The corresponding optimized surface structures are shown in Fig. 3a. Single-point energy calculations (Table S2†) were performed at high-symmetry adsorption sites for oxygen, including hexagonal close-packed (hcp) and face-centered cubic (fcc) configurations, yielding four distinct O-terminated structures: hcp–fcc, fcc–hcp, fcc–fcc, and hcp–hcp, as shown in Fig. 3b and c. The results demonstrate that hcp–hcp sites are generally energetically favorable in MXenes, except for $Cr_2Ti_2C_3O_2$, $Cr_2V_2C_3O_2$ and $Cr_2Ta_2C_3O_2$, where fcc–fcc configurations are preferred. Band structure calculations demonstrate excellent electrical conductivity for these 19 configurations (Fig. S2†), enhancing charge transfer performance and improving HER efficiency.

3.2. Simulating Gibbs free energy of hydrogen adsorption

$|\Delta G_H|$ serves as a key descriptor for evaluating catalytic activity in HER catalysts. For these calculations, we utilized a 2 × 2 × 1 supercell configuration, examining 19 O-terminated MXenes with 25% hydrogen coverage. The choice of 1/4 hydrogen coverage is based on the calculation results that, in most cases, DTM MXenes exhibit stable hydrogen adsorption at this level

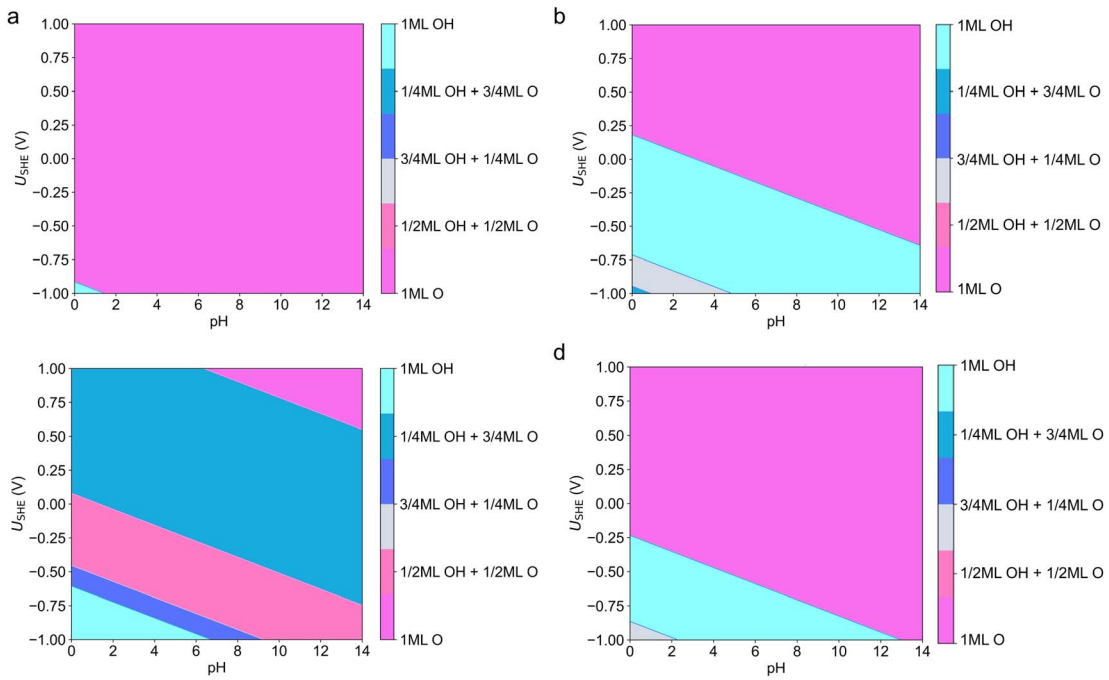

Fig. 2 Surface Pourbaix diagrams of (a) Cr_2TiC_2, (b) Mo_2TiC_2, (c) $Ti_2Ta_2C_3$ and (d) $W_2Hf_3C_2$. The most thermodynamically stable states of the surface under relevant U_{SHE} conditions and pH values are labeled by the terminations.

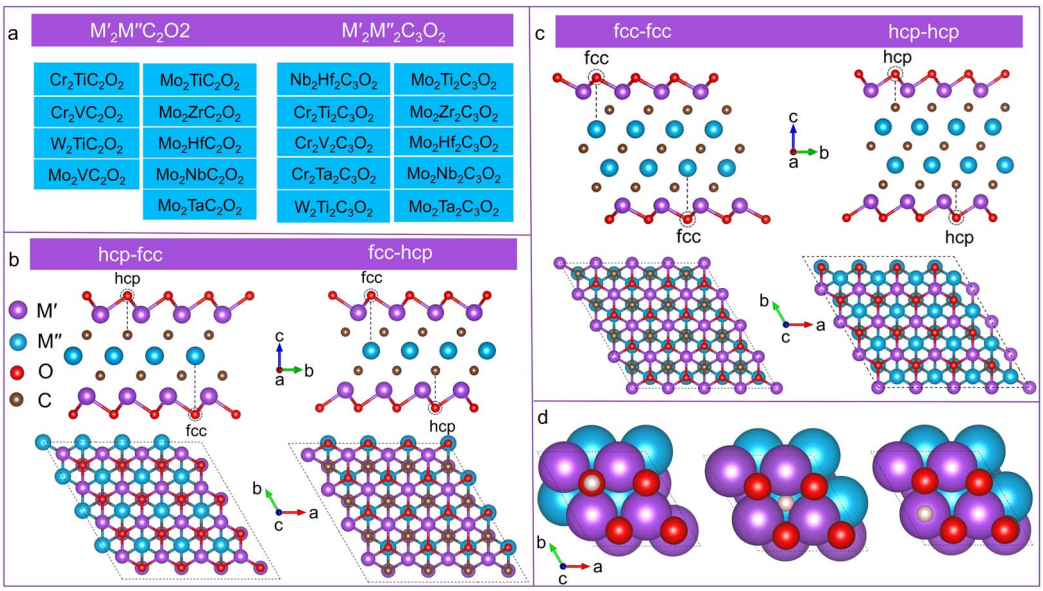

Fig. 3 Crystal structures. (a) List of 9 $M'_2M''C_2O_2$ and 10 $M'_2M''_2C_3O_2$, demonstrated to be synthesizable, stable and conductive, are investigated in this work for the HER. (b and c) Atomic structures of $M'_2M''C_2O_2$ in hcp–fcc and fcc–hcp types and $M'_2M''_2C_3O_2$ in fcc–fcc and hcp–hcp types viewed from the top and side, respectively. (d) Top view of three distinct adsorption structures for 1/4 hydrogen coverage on MXenes.

within a potential window of −1 V to −1 V, as supported by Pourbaix diagram analyses (as shown in Fig. 4). Hydrogen atoms are positioned at the top of surface functional groups (O), hcp, and fcc sites, respectively, as illustrated in the left panel of Fig. 3d. Our results indicate that hydrogen is more stable when adsorbed onto the top O site, aligning with previous studies.[11,13]

The Gibbs free energies for the adsorption of atomic hydrogen, ΔG_H, on the 9 $M'_2M''C_2O_2$ and 10 $M'_2M''_2C_3O_2$ structures have been calculated, as shown in Fig. 5a and 2b. Our results indicate that 4 $M'_2M''C_2O_2$ and 4 $M'_2M''_2C_3O_2$ structures exhibit theoretical $|\Delta G_H|$ values below 0.2 eV, indicating their potential as HER electrocatalysts.[6] The most promising

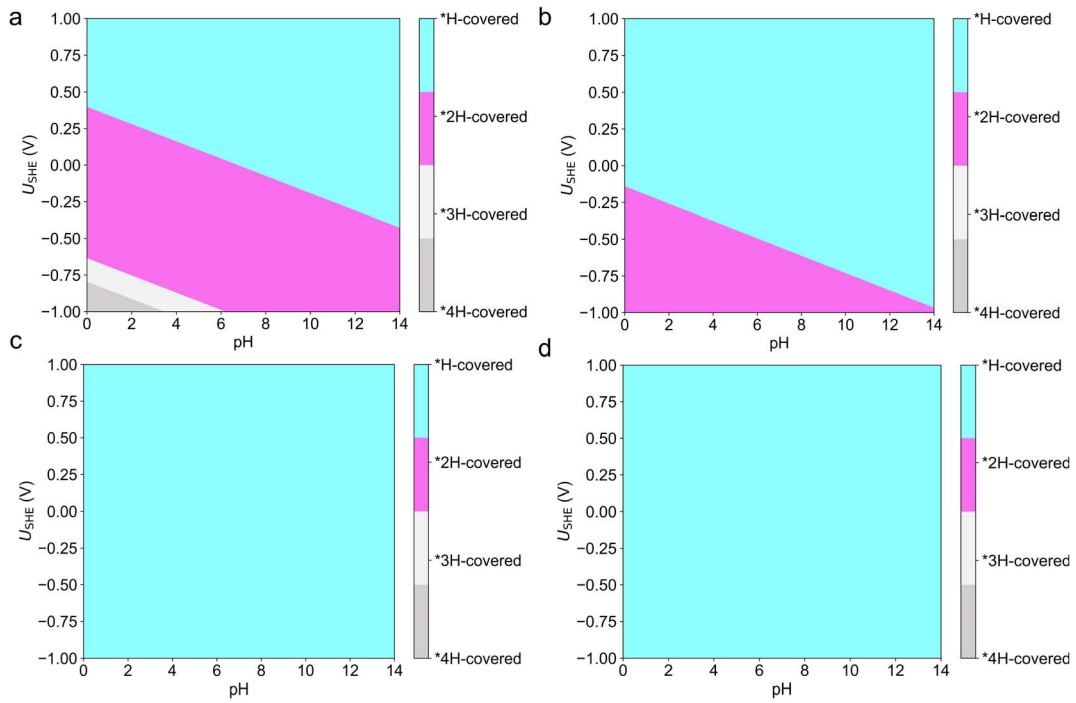

Fig. 4 The surface Pourbaix diagrams as a function of pH and potential under different hydrogen coverage. Surface Pourbaix diagrams of (a) $Cr_2TiC_2O_2$, (b) $Mo_2TiC_2O_2$, (c) $W_2Hf_2C_3O_2$ and (d) $W_2Zr_2C_3O_2$.

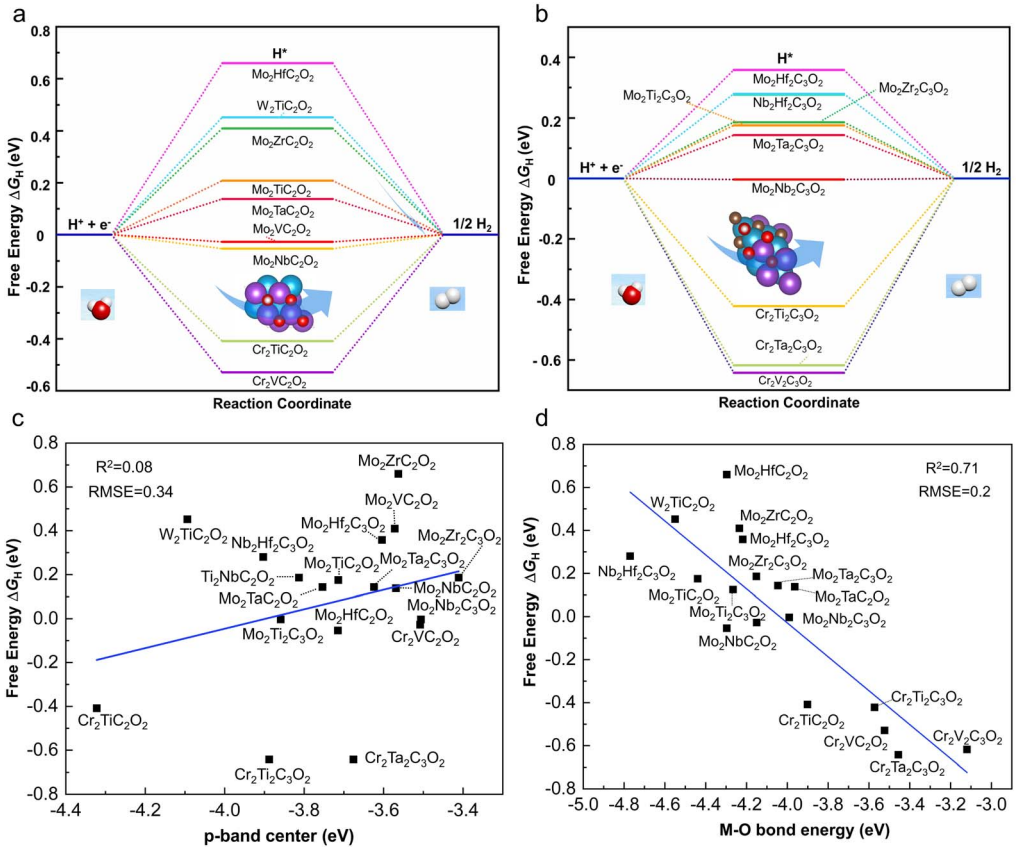

Fig. 5 (a and b) HER free energy diagrams of $M'_2M''C_2O_2$, and $M'_2M''_2C_3O_2$ under standard conditions, respectively. (c and d) Relationships between ΔG_H and descriptors including (c) the p-band center of the oxygen functional group and (d) the bond energy between the first-layer transition metal and oxygen of different MXene systems, respectively.

candidate is $Mo_2Nb_2C_3O_2$, which shows the lowest theoretical overpotential (−0.004 eV). Notably, all identified HER electrocatalysts are Mo-based MXenes, including $Mo_2Nb_2C_3O_2$, $Mo_2VC_2O_2$, $Mo_2NbC_2O_2$, $Mo_2Ti_2C_3O_2$, $Mo_2TaC_2O_2$, $Mo_2Ta_2C_3O_2$, $Mo_2TiC_2O_2$ and $Mo_2Zr_2C_3O_2$. Our DFT calculations have identified Mo-based ordered DTM MXene structures as promising HER electrocatalysts. With the increasing synthesis of Mo-based MXenes in laboratory settings, our work is poised to contribute to their expanding applications in catalysis.[42,44]

3.3. Proposing a descriptor for the HER activity

While ΔG_H evaluates the activity of the HER, it fails to account for intrinsic structural characteristics. Furthermore, DFT calculations can be resource-intensive. To address this issue, several descriptors were tested to correlate with the HER activity of MXenes. Based on correlation coefficients and error metrics, we found that none of the descriptors, including the p-band center of oxygen ($R^2 = 0.08$) (as shown in Fig. 5c) and the d-band center of the first-layer transition metal ($R^2 = 0.01$) (as shown in Fig. S3†), could adequately describe the HER activity of MXenes. Only the bond energy between the first-layer transition metal and oxygen exhibited a slightly higher correlation ($R^2 = 0.71$), as detailed in Fig. 5d. The reason for this is that the MXene system involves multi-layer atomic interactions, including various early transition metals interacting with carbon and oxygen atoms. Thus, a single descriptor cannot fully capture its hydrogen evolution activity, and a more comprehensive descriptor is required to properly describe the structure–activity relationship of MXenes.

To address this issue, we aim to propose a direct and cost-effective structural descriptor specifically for ordered DTM MXenes.

3.3.1. The orbital hybridization during chemisorption. We started with the exploration of the hydrogen adsorption mechanism on MXenes and tried to dig out the determining factors for adsorption energy. Therefore, we systematically investigate its orbital hybridization during chemisorption. For the H-MXene system, the p_z orbital of oxygen interacts with the s orbital of hydrogen, facilitating H–O bond formation, as shown by the projected crystal orbital Hamilton population (pCOHP) analysis in Fig. S5 and S6.† Additionally, the p_x and p_y orbitals of oxygen bond with the d orbitals of the outer metal layer (M′), contributing to M′–O bonding.

Taking $Mo_2TiC_2O_2$ as a representative example, the orbital interactions of M′–O bonding are analyzed by the projected density of states (pDOS) and the pCOHP (Fig. 6a), and it is illustrated in Fig. 6b, with two bonding and antibonding orbitals, respectively. This analysis involved a detailed examination of the overlap peaks in the pDOS for both Mo and O,

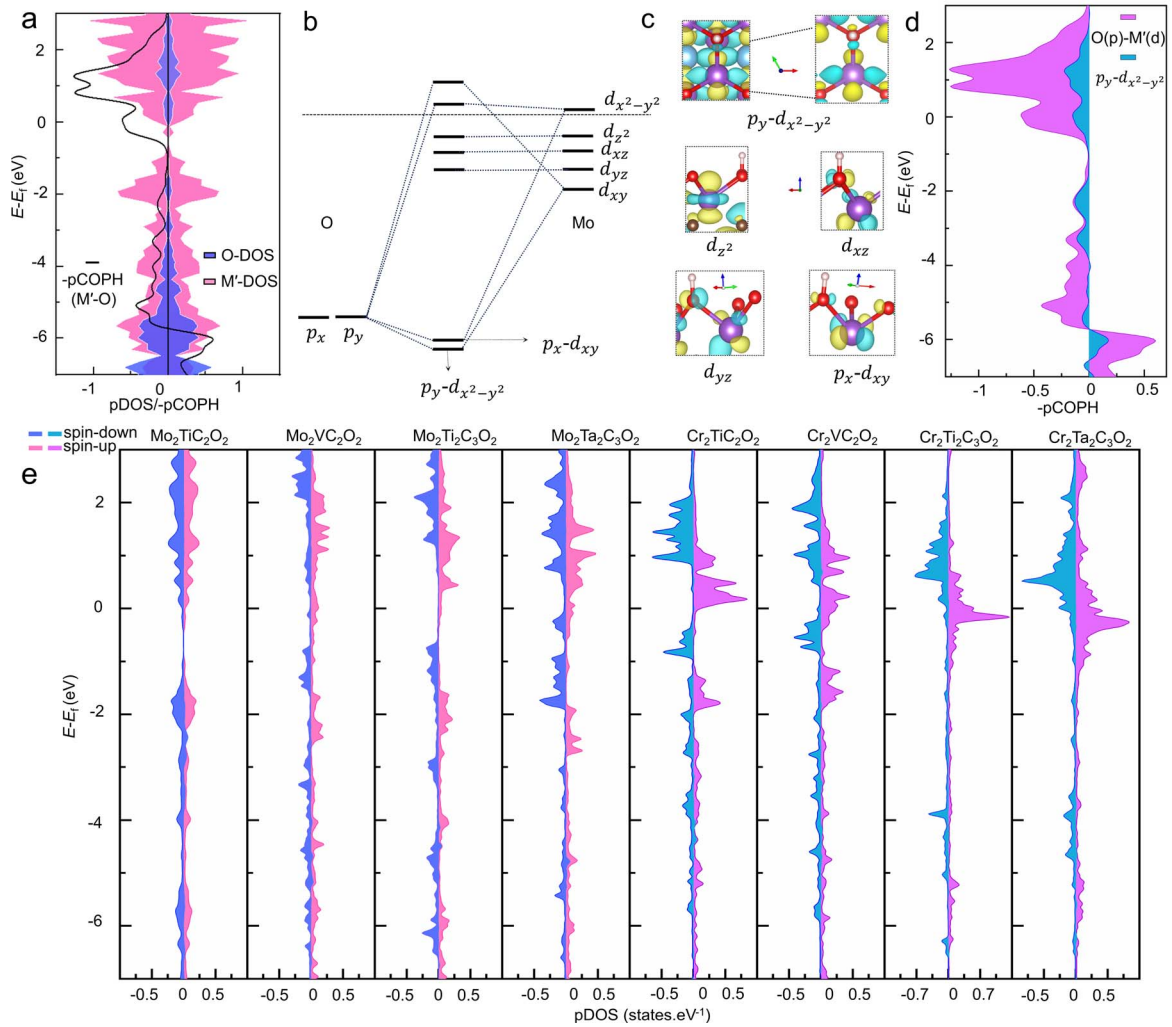

Fig. 6 (a) The projected density of states (pDOS) analysis (red curve: M′(Mo) and purple curve: O) as well as pCOHP analysis of the M′(Mo)–O bond. (b) Spin-down and spin-up interactions of the Mo orbital with the O orbital, with (c) post-interaction corresponding wave functions. (d) pCOHP of the Mo(p)–O(d) bond and its O (p_y)–Mo ($d_{x^2-y^2}$) component (red curve: Mo(p)–O(d) and blue curve: p_y-$d_{x^2-y^2}$). (e) pDOS plots of the $d_{x^2-y^2}$ orbital for eight distinct MXenes materials, respectively.

combined with the bonding and anti-bonding characteristics of the Mo–O bond as well as the wave function image shown in Fig. 6c, ranging from −7 eV to 3 eV. Furthermore, our results show that the O(p_y)–Mo($d_{x^2-y^2}$) component mainly contributes to the Mo–O bond formation (supported by COHP in Fig. 6d). Additionally, the pCOHP analysis for other MXenes further supports the above conclusion, as shown in Fig. S6.†

To investigate the role of $d_{x^2-y^2}$ orbitals in outer transition metals, we examined it across eight types of Mo- and Cr-based MXenes to ensure a diverse range of systems (Fig. 6e). The results reveal that Cr-based MXenes exhibit significantly localized $d_{x^2-y^2}$ orbitals at the Fermi level, indicating stronger interactions with O (p_y) orbitals forming a σ bond. Meanwhile, this σ (O_{p_y}–M′$d_{x^2-y^2}$) state would strongly interact with the σ (H_s–O_{p_z}) state, leading to stronger H adsorption with reduced HER activity. These findings suggest that the $d_{x^2-y^2}$ orbital of outer transition metals plays a critical role in the M′–O bond formation and HER performance across various MXenes.

3.3.2. Linking Gibbs free energy with O–H bond dissociation enthalpy. From a microscopic perspective, the $d_{x^2-y^2}$ orbitals of outer transition metals are critical determinants for HER performance. However, can this be validated from a macroscopic standpoint? In this study, we aim to expand upon ΔG_H and correlate it with structural and electronic features. The effective criterion ΔG_H can also be expressed as follows:

$$\Delta G_H = \Delta H_H - T\Delta S \quad (5)$$

Here, ΔH_H represents the change in bond dissociation enthalpies (BDE) during the chemical reaction. Specifically, in this study, it refers to the enthalpy change associated with hydrogen adsorption during the Volmer reaction: $H^+(aq) + e^- + * \rightarrow H^*$. Therefore, ΔH_H can be further defined in eqn (6), where ΔH(MXene) and ΔH(H) denote the BDE of the reactants, which are zero since they are stable, while ΔH(MXene–H)

represents the BDE of the product. Here, the BDE of the MXene–H bond is approximately equal to that of the O–H bond, as hydrogen atoms preferentially bind to surface O sites upon adsorption on MXenes. This bonding configuration is evidenced by pDOS and pCOHP (Fig. S5†).

$$\begin{aligned}\Delta H_{\mathrm{H}} &= \mathrm{BDE(MXene)} + \mathrm{BDE(H)} - \mathrm{BDE(MXene\text{–}H)} \\ &= -\mathrm{BDE(MXene\text{–}H)} \approx -\mathrm{BDE(`O'\text{–}H)}\end{aligned} \tag{6}$$

3.3.3. Expanding O–H bond dissociation enthalpy *via* Pauling electronegativity. As shown in Fig. 7a, when hydrogen adsorbs onto MXenes, electron transfer occurs between the hydrogen and oxygen atoms, as well as among other atoms in the MXene system. To analyze this charge transfer process, Bader charge analysis was performed, focusing on the electron transfer within the O–H bond, as depicted in Fig. 7b. The results indicate that, despite variations among MXenes, the charge transfer from hydrogen to MXene aligns closely with the Pauling electronegativity ratio between hydrogen and oxygen ($\chi_{\mathrm{H}}/\chi_{\mathrm{O}} = 0.6395$), suggesting that electronegativity differences primarily drive charge transfer, with material's other structural properties playing a secondary role.

Based on the relationship between BDE and electronegativity in the Pauling electronegativity formula (eqn (S1)†),[45,46] the BDE of the O–H bond is expanded as follows:

$$\Delta H_{\mathrm{H}} \approx -\mathrm{BDE(`O'-H)} = -\frac{\mathrm{BED}\left(\mathrm{M}' - \mathrm{O}\right) + \mathrm{BED(H-H)}}{2} - (\chi_{\mathrm{O}} - \chi_{\mathrm{H}})^2 + \mathrm{X}' \tag{7}$$

In eqn (7), an approximation has been made by replacing the BDE (O–O) with BDE (M′–O). This substitution is essential as it takes the complex structural features of 2D MXene multilayers into account. Given that M′ is chemically bonded to O, this approximation provides a more accurate representation of the system's behavior and is thus a necessary step in our analysis. It has been well-established, both in our current work and prior studies,[11,15] that the outer-layer metals (M′) in MXenes are significantly involved in catalytic activity. X′ acts as a correction

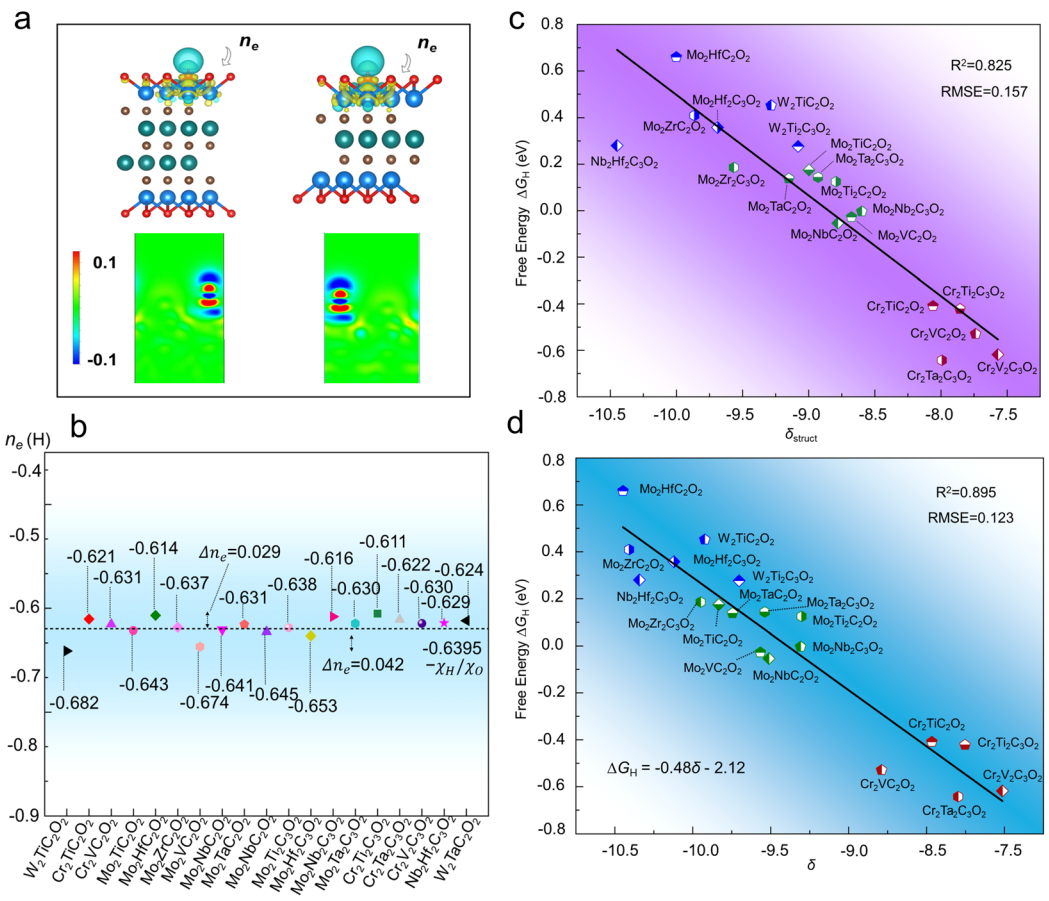

Fig. 7 (a) The top panel is the charge density difference plots for H adsorbed on $Mo_2Ti_2C_3O_2$ and $Mo_2TiC_2O_2$ with an isosurface value of 0.0004 e bohr^{-3}, respectively, and blue and yellow represent charge loss and charge accumulation, respectively. Bottom panel is the sliced electron localization function (ELF) of H adsorbed on $Mo_2Ti_2C_3O_2$ and $Mo_2TiC_2O_2$ monolayers along the (001) plane, respectively. (b) The transfer of charges from hydrogen to the oxygen functional group on MXene varies depending on the material, as evaluated by Bader charge analysis. (c) Relationships between ΔG_H and descriptor δ_{struct} of different MXenes. (d) Relationships between ΔG_H and descriptor δ of different MXene systems.

factor in the ΔH_H calculations to account for other structural influences of MXenes. Using this expanded formula, a descriptor (δ_1) is developed for HER catalytic activity, incorporating an additional correction factor (X), as shown in eqn (8):

$$\delta_1 = -\frac{\mathrm{BED}\left(\mathrm{M}^{'}-\mathrm{O}\right)+\mathrm{BED}(\mathrm{H}-\mathrm{H})}{2}-\left(\chi_{\mathrm{O}}-\chi_{\mathrm{H}}\right)^2+\mathrm{X} \quad (8)$$

As a result, the outer-layer metals determine the BDE(M′–O) values, therefore, influencing δ_1 values and HER activities, and the values of BDE(M′–O) are listed in Table S3.† The finding is consistent with the previous conclusion that the outer metal layer ($d_{x^2-y^2}$ orbital) plays an important role in the HER. Therefore, the crucial role of outer-layer metals in modulating HER performance explains why all identified HER electrocatalysts in this study are Mo-based MXenes, both from microscopic and macroscopic perspectives.

3.3.4. Optimizing descriptors through structural characteristics. While the outer-layer transition metal is crucial, other structural features, such as the inner-layer transition metal and the number of transition metal layers, are also vital for developing effective descriptors for HER activity. Variations in the inner-layer transition metals, as seen in $Mo_2TiC_2O_2$ and $Mo_2VC_2O_2$ or $Cr_2Ti_2C_3O_2$ and $Cr_2Ta_2C_3O_2$, lead to notable differences in the $d_{x^2-y^2}$ orbital characteristics of the outer transition metal. Furthermore, for the same combination of inner and outer transition metals, increasing the number of layers enhances the localization of $d_{x^2-y^2}$ orbital electrons at the Fermi level, as evidenced by comparisons of $Mo_2TiC_2O_2$ and $Mo_2Ti_2C_3O_2$, as well as $Cr_2TiC_2O_2$ and $Cr_2Ti_2C_3O_2$. Given that the $d_{x^2-y^2}$ orbital significantly influences HER performance, the roles of both the inner-layer transition metal and the number of transition metal layers are critical.

Our calculations confirm that ΔG_H varies with different inner transition metal layers for the same outer transition metal layer MXenes. Specifically, ΔG_H decreases with the increasing electronegativity of the inner transition metal and varies with the number of inner transition metal layers, as illustrated in Fig. S7.† This indicates that both the electronegativity of the inner transition metal and the number of inner transition metal layers should be incorporated into the descriptor. Therefore, we propose the correction factor $(\chi_{M''}-\chi_C)^2\times(2.05-2n)$ as $\delta_{correct}$. The term $(\chi_{M''}-\chi_C)^2$ characterizes the bonding influence of the inner transition metal M″ on the carbon atoms, employing an expression analogous to that in eqn (8). Besides, $(2.05-2n)$ serves as the layer influence factor corresponding to its structural characteristics, where 2.05 is derived from the approximate axial ratio coefficient ($c/2a$), and n represents the number of layers of the inner transition metal. The lattice constants of the considered MXenes are illustrated in Table S4.† Thus, the descriptor δ_{struct} is expressed as $\delta_1+\delta_{correct}$, which is defined as,

$$\delta_{struct} = -\frac{\mathrm{BED}\left(\mathrm{M}^{'}-\mathrm{O}\right)+\mathrm{BED}(\mathrm{H}-\mathrm{H})}{2}-\left(\chi_{\mathrm{O}}-\chi_{\mathrm{H}}\right)^2-\left(\chi_{\mathrm{M}''}-\chi_{\mathrm{C}}\right)^2\times(2.05-2n) \quad (9)$$

The scaling relationship between ΔG_H and the structural descriptor δ_{struct} is shown in Fig. 7c, characterized by a coefficient of determination ($R^2=0.82$), which underscores the effectiveness of the descriptor in representing HER activity in oxygen-functionalized MXenes.

3.3.5. Incorporating charge transfer-induced energy changes into descriptors. Complementary to structural characteristics, incorporating electronic properties into descriptors is crucial for accurately assessing hydrogen adsorption energy on MXenes. We introduced a two-stage model to elucidate the electron transfer mechanism during O–H bond formation. In the initial stage, an electron is ionized from the hydrogen atom, incurring an energy cost equivalent to its ionization energy (E_{IE}). This electron is then transferred to an oxygen functional group on the MXene surface. Given MXenes' metallic nature (with no band gap, as shown in Fig. S2†), the work function (Φ) serves as an essential parameter for quantifying charge transfer. The charge transfer energy descriptor (δ_{tran}) is defined as $\chi_H/\chi_O\,(E_{IE}-\Phi)$, where the hydrogen-to-oxygen electronegativity ratio (χ_H/χ_O) approximates the electron transfer quantity (n), indicating net electron transfer from hydrogen to the catalyst, as verified by Bader charge analysis. This results in a comprehensive descriptor, $\delta=\delta_{struct}+\delta_{tran}$, for evaluating ΔG_H in the HER on ordered DTM MXenes:

$$\delta = -\frac{\mathrm{BED}\left(\mathrm{M}^{'}-\mathrm{O}\right)+\mathrm{BED}(\mathrm{H}-\mathrm{H})}{2}-\left(\chi_{\mathrm{O}}-\chi_{\mathrm{H}}\right)^2-\left(\chi_{\mathrm{M}''}-\chi_{\mathrm{C}}\right)^2\times(2.05-2n)+\chi_{\mathrm{H}}/\chi_{\mathrm{O}}\,(E_{\mathrm{IE}}-\Phi) \quad (10)$$

This descriptor captures the sequential steps in electron transfer, offering insight into energy dynamics. The linear correlation between δ and ΔG_H (Fig. 7d), expressed as $\Delta G_H=-0.48\delta-2.12$, shows improved accuracy with an R^2 increase from 0.825 to 0.895 and RMSE reduction from 0.157 to 0.123.

3.3.6. Evaluating the efficacy of descriptors. DFT calculations on 12 additional ordered double transition metal materials in the database,[47] including W-, Ti-, Hf-, Nb-, and V-based MXenes, are conducted to assess the generalizability of the proposed descriptor (δ). As shown in Fig. 8, the results reveal a consistent linear relationship between δ and ΔG_H, expressed as $\Delta G_H=-0.49\delta-2.18$, with minimal coefficient variation (from −0.48 to −0.49 and −2.12 to −2.18) compared to the model ($\Delta G_H=-0.48\delta-2.12$). This demonstrated the descriptor's universality in predicting HER activity for ordered DTM MXenes. The model achieved a high coefficient of determination ($R^2=0.900$) and a root mean square error (RMSE) of 0.122, confirming its robustness. Although outlier points were not excluded in the present analysis, future studies may benefit from systematic outlier detection and removal strategies to enhance the robustness of the scaling relationship, as suggested in recent studies.[48,49] Additionally, new HER candidates such as $Ti_2Nb_2C_3O_2$ (−0.08 eV), $Ti_2TaC_2O_2$ (−0.189 eV), and $Nb_2Ta_2C_3O_2$(−0.152 eV) were identified by these DFT calculations.

To evaluate the generalizability of the proposed descriptor, we conducted an extension study in the application of the

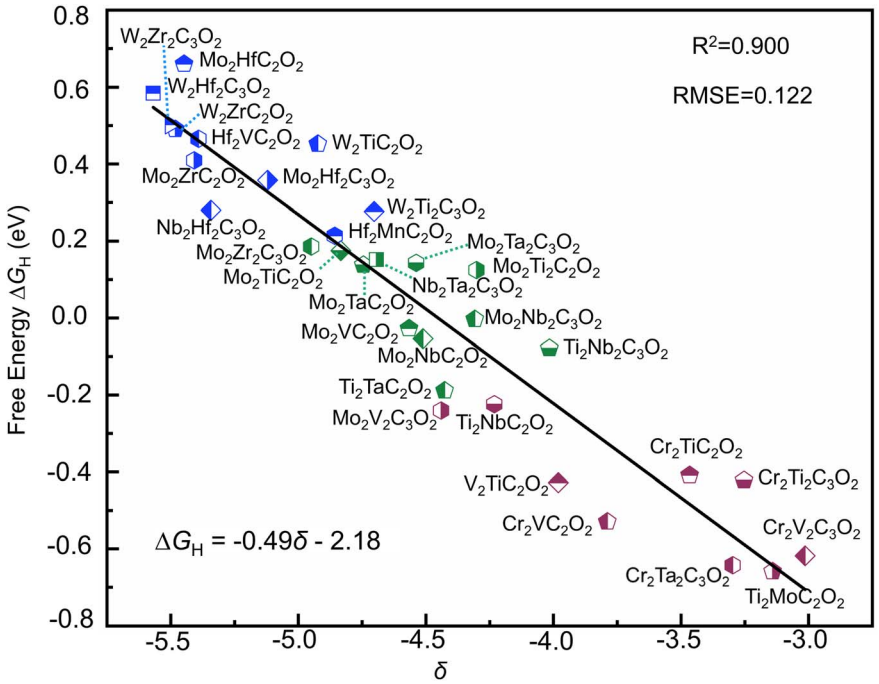

Fig. 8 Relationships between ΔG_H and descriptor δ in the 31 different MXene systems.

descriptor, especially in the $M'_2M''N_2O_2$ system, where C electronegativity is substituted with N electronegativity and the lattice coefficient is adjusted to 2.5, while keeping all other variables constant. This modification makes the descriptor more accurate for predicting ΔG_H in the $M'_2M''N_2O_2$ system. We randomly selected and tested nearly 20 materials in the $M'_2M''N_2O_2$, which were later validated using DFT. The results revealed a relatively strong linear correlation between the descriptor and ΔG_H, with an R^2 of 0.81, as shown in Fig. S8.† This finding not only validates the effectiveness of the descriptor but also demonstrates its applicability across different systems, highlighting its potential for broader use in similar MXene structures.

3.3.7. Predicting Gibbs free energy by using descriptors. To further demonstrate the efficiency of the descriptor δ in accelerating the search for potential HER materials, it is applied to rapidly screen the promising HER catalyst satisfying $|\Delta G_H| < 0.2$ eV among the remaining 16 types of theoretical ordered DTM materials.[47] In order to obtain the descriptor δ as shown in eqn (10), DFT calculations are only performed to obtain the Φ value of the MXene. Using the model $\Delta G_H = -0.49\delta - 2.18$, $Ti_2MnC_2O_2$ (0.08 eV) and $Ti_2Ta_2C_3O_2$ (−0.12 eV) are predicted as promising HER catalysts. Subsequent DFT calculations validated these predictions with acceptable deviations. For $Ti_2MnC_2O_2$, the DFT-calculated ΔG_H is 0.1 eV, showing a minor error of 0.02 eV compared to the predicted value. Similarly, for $Ti_2Ta_2C_3O_2$, the DFT-calculated ΔG_H is −0.06 eV, with an error of 0.06 eV. These results demonstrate the model's reliability in predicting catalyst performance within a reasonable margin of error. Thus, the descriptor δ proves to be a reliable and efficient tool for screening potential HER materials.

3.4. Optimizing catalysis with implicit solvation models

Surface electrocatalysis at solid–liquid interfaces is inherently complex, necessitating consideration of liquid electrolyte species within the finite volume between periodically repeating slabs.[50] To address this issue, the implicit and explicit solvation models are always considered in the calculation of ΔG_H, and the explicit solvation model is always more accurate for the representation of solvation effects. However, in this study, we use an implicit solvation model to correct the adsorption free energies based on accuracy tests, with detailed information provided in Fig. S9 and Table S5.† The theoretical overpotentials for $Mo_2TiC_2T_X$ in solutions with pH values of 0, 0.3, 1, and 2 are approximately −0.39 V, −0.41 V, −0.45 V, and −0.51 V, respectively. These values align well with experimentally reported overpotentials of −0.39 V, −0.40 V, −0.45 V, and −0.47 V, underscoring the necessity of incorporating the implicit solvation model.[37]

The results show that the solvent has a significant impact on the adsorption free energies; detailed data are shown in Table S6.† The electrostatic screening of the solvent at the surface leads to a reduction of about 0.5 eV in adsorption energy across most ordered DTM MXene systems during hydrogen adsorption. In particular, $Mo_2HfC_2O_2$ exhibits a significant energy reduction of 1.338 eV. This surface, in particular, has a higher proportion of ionic bonds in the formation of polar covalent H–O bonds, which leads to a notable energy reduction.[27] The calculated value of ΔG_H is implied by the equation $\Delta G_H = \Delta E_H + \Delta E_{ZPE} + \Delta U_{\tilde{0}T} - T\Delta S + k_B T \ln 10 \times PH$ in our work, where κ_B is the Boltzmann constant, and T is set to 298.15 K. The dielectric constant ε_{bulk} in the implicit solvation model is 78.4, the experimental value for liquid water at 298 K.

The solvent environment significantly impacts the calculated ΔG_H, thus requiring a rescreening for $|\Delta G_H| < 0.2$ eV *via* an implicit solvation model. Given that ΔG_H generally diminishes by approximately 0.5 eV with the implicit solvation model, we elected to recompute materials whose initial ΔG_H values lay within the range of 0.2 eV to 0.8 eV, as certain materials were prone to fall outside the requisite value range. This resulted in four promising candidates: $Mo_2Nb_2C_3O_2$, $Mo_2Hf_2C_3O_2$, $W_2Hf_2C_3O_2$, and $W_2Zr_2C_3O_2$,each exhibiting $|\Delta G_H|$ values below 0.2 eV. *Ab initio* molecular dynamics (AIMD) simulations at 300 K, along with phonon band structure analysis, confirmed their mechanical and thermal stability (Fig. S10†). Additionally, the synthesizability of these materials is evaluated by demonstrating the stability of the precursor MAX phase as detailed in Table S1.† In a word, these four compounds are considered promising candidates for experimental synthesis.

4. Conclusions

This study developed a screening strategy to identify promising catalysts among ordered DTM MXenes, with four Mo- and W-based systems emerging as strong HER candidates for experimental validation. This approach considers key factors such as synthesizability, stability, and conductivity of MXenes, which are essential for practical applications. A universal screening descriptor is introduced, and its linear relationship with ΔG_H ($\Delta G_H = -0.49\delta - 2.18$) demonstrates its broad applicability, facilitating efficient screening of MXene catalysts for the HER. The descriptor not only deepens the understanding of structure–activity relationships, particularly highlighting the critical role of $M'(d_{x^2-y^2})$–$O(p_y)$ orbital interactions in governing catalytic performance, but also bridges to accessible structural and electronic features such as bond dissociation energy, electronegativity, lattice parameters, ionization energy, and work function. It simultaneously enables efficient screening of MXene-based catalysts and elucidates the underlying mechanisms of their catalytic behavior. The framework and methodology behind this descriptor provide a strategic roadmap for the descriptor development and efficient catalyst screening across diverse material systems.

Data availability

The data supporting this article have been included as part of the ESI.†

Author contributions

Junmei Du designed the study, performed the research, analyzed the data, and wrote the manuscript. Yifan Yan, Xiumei Li and Jiao Chen analyzed the data. Chunsheng Guo revised the manuscript. Yuanzheng Chen and Hongyan Wang designed the study and revised the manuscript.

Conflicts of interest

There are no conflicts to declare.

Acknowledgements

This work was supported by the National Natural Science Foundation of China (12164009) and the Sichuan Science and Technology program (2022ZYD0024 and 2021YFG0228).

References

1 J. A. Turner, Sustainable Hydrogen Production, *Science*, 2004, **305**, 972–974.
2 I. Roger, M. A. Shipman and M. D. Symes, Earth-abundant catalysts for electrochemical and photoelectrochemical water splitting, *Nat. Rev. Chem.*, 2017, **1**, 0003.
3 M. Ball and M. Weeda, The hydrogen economy - Vision or reality?, *Int. J. Hydrogen Energy*, 2015, **40**, 7903–7919.
4 X. Zhao, Z. H. Levell, S. Yu and Y. Liu, Atomistic understanding of two-dimensional electrocatalysts from first principles, *Chem. Rev.*, 2022, **122**, 10675–10709.
5 C. G. Morales-Guio, L.-A. Stern and X. Hu, Nanostructured hydrotreating catalysts for electrochemical hydrogen evolution, *Chem. Soc. Rev.*, 2014, **43**, 6555–6569.
6 J. Greeley, T. F. Jaramillo, J. Bonde, I. Chorkendorff and J. K. Nørskov, Computational high-throughput screening of electrocatalytic materials for hydrogen evolution, *Nat. Mater.*, 2006, **5**, 909–913.
7 X. Zou and Y. Zhang, Noble metal-free hydrogen evolution catalysts for water splitting, *Chem. Soc. Rev.*, 2015, **44**, 5148–5180.
8 N. Ramaswamy, U. Tylus, Q. Jia and S. Mukerjee, Activity descriptor identification for oxygen reduction on nonprecious electrocatalysts: linking surface science to coordination chemistry, *J. Am. Chem. Soc.*, 2013, **135**, 15443–15449.
9 Z. W. Seh, J. Kibsgaard, C. F. Dickens, I. Chorkendorff, J. K. Nørskov and T. F. Jaramillo, Combining theory and experiment in electrocatalysis: Insights into materials design, *Science*, 2017, **355**, eaad4998.
10 B. Anasori, Y. Xie, M. Beidaghi, J. Lu, B. C. Hosler, L. Hultman, P. R. C. Kent, Y. Gogotsi and M. W. Barsoum, Two-dimensional, ordered, double transition metals carbides (MXenes), *ACS Nano*, 2015, **9**, 9507–9516.
11 R. Anand, A. S. Nissimagoudar, M. Umer, M. Ha, M. Zafari, S. Umer, G. Lee and K. S. Kim, Late transition metal doped MXenes showing superb bifunctional electrocatalytic activities for water splitting via distinctive mechanistic pathways, *Adv. Energy Mater.*, 2021, **11**, 2102388.
12 I. Hussain, U. Sajjad, O. J. Kewate, U. Amara, F. Bibi, A. Hanan, D. Potphode, M. Ahmad, M. S. Javed, P. Rosaiah, S. Hussain, K. Khan, Z. Ajmal, S. Punniyakoti, S. S. Alarfaji, J.-H. Kang, W. Al Zoubi, S. Sahoo and K. Zhang, Double transition-metal MXenes: classification, properties, machine learning, artificial intelligence, and energy storage applications, *Mater. Today Phys.*, 2024, **42**, 101382.
13 Z. Zeng, X. Chen, K. Weng, Y. Wu, P. Zhang, J. Jiang and N. Li, Computational screening study of double transition

metal carbonitrides $M'_2M''CNO_2$-MXene as catalysts for hydrogen evolution reaction, *npj Comput. Mater.*, 2021, **7**, 80.
14 Y.-W. Cheng, J.-H. Dai, Y.-M. Zhang and Y. Song, Two-dimensional, ordered, double transition metal carbides (MXenes): A new family of promising catalysts for the hydrogen evolution reaction, *J. Phys. Chem. C*, 2018, **122**, 28113–28122.
15 D. Jin, L. R. Johnson, A. S. Raman, X. Ming, Y. Gao, F. Du, Y. Wei, G. Chen, A. Vojvodic, Y. Gogotsi and X. Meng, Computational screening of 2D ordered double transition-metal carbides (MXenes) as electrocatalysts for hydrogen evolution reaction, *J. Phys. Chem. C*, 2020, **124**, 10584–10592.
16 X. Wang, C. Wang, S. Ci, Y. Ma, T. Liu, L. Gao, P. Qian, C. Ji and Y. Su, Accelerating 2D MXene catalyst discovery for the hydrogen evolution reaction by computer-driven workflow and an ensemble learning strategy, *J. Mater. Chem. A*, 2020, **8**, 23488–23497.
17 J. Zheng, X. Sun, C. Qiu, Y. Yan, Z. Yao, S. Deng, X. Zhong, G. Zhuang, Z. Wei and J. Wang, High-throughput screening of hydrogen evolution reaction catalysts in MXene materials, *J. Phys. Chem. C*, 2020, **124**, 13695–13705.
18 N. Dubouis and A. Grimaud, The hydrogen evolution reaction: from material to interfacial descriptors, *Chem. Sci.*, 2019, **10**, 9165–9181.
19 W. Jiang, X. Zou, H. Du, L. Gan, C. Xu, F. Kang, W. Duan and J. Li, Universal descriptor for large-scale screening of high-performance MXene-based materials for energy storage and conversion, *Chem. Mater.*, 2018, **30**, 2687–2693.
20 L. Chen, Y. Tian, X. Hu, S. Yao, Z. Lu, S. Chen, X. Zhang and Z. Zhou, A Universal machine learning framework for electrocatalyst innovation: A case study of discovering Alloys for hydrogen evolution reaction, *Adv. Funct. Mater.*, 2022, **32**, 2208418.
21 L. Chen, X. Zhang, A. Chen, S. Yao, X. Hu and Z. Zhou, Targeted design of advanced electrocatalysts by machine learning, *Chin. J. Catal.*, 2022, **43**, 11–32.
22 B. M. Abraham, P. Sinha, P. Halder and J. K. Singh, Fusing a machine learning strategy with density functional theory to hasten the discovery of 2D MXene-based catalysts for hydrogen generation, *J. Mater. Chem. A*, 2023, **11**, 8091–8100.
23 G. Kresse and J. Furthmüller, Efficient iterative schemes for ab initio total-energy calculations using a plane-wave basis set, *Phys. Rev. B:Condens. Matter Mater. Phys.*, 1996, **54**, 11169–11186.
24 J. P. Perdew, K. Burke and M. Ernzerhof, Generalized gradient approximation made simple, *Phys. Rev. Lett.*, 1996, **77**, 3865–3868.
25 G. Kresse and D. Joubert, From ultrasoft pseudopotentials to the projector augmented-wave method, *Phys. Rev. B:Condens. Matter Mater. Phys.*, 1999, **59**, 1758–1775.
26 S. Grimme, Semiempirical GGA-type density functional constructed with a long-range dispersion correction, *J. Comput. Chem.*, 2006, **27**, 1787–1799.
27 S. Grimme, S. Ehrlich and L. Goerigk, Effect of the damping function in dispersion corrected density functional theory, *J. Comput. Chem.*, 2011, **32**, 1456–1465.
28 D. Gunceler, K. Letchworth-Weaver, R. Sundararaman, K. A. Schwarz and T. A. Arias, The importance of nonlinear fluid response in joint density-functional theory studies of battery systems, *Modell. Simul. Mater. Sci. Eng.*, 2013, **21**, 074005.
29 K. Mathew, V. S. C. Kolluru, S. Mula, S. N. Steinmann and R. G. Hennig, Implicit self-consistent electrolyte model in plane-wave density-functional theory, *J. Chem. Phys.*, 2019, **151**, 234101.
30 K. Mathew, R. Sundararaman, K. Letchworth-Weaver, T. A. Arias and R. G. Hennig, Implicit solvation model for density-functional study of nanocrystal surfaces and reaction pathways, *J. Chem. Phys.*, 2014, **140**, 084106.
31 R. Nelson, C. Ertural, J. George, V. L. Deringer, G. Hautier and R. Dronskowski, LOBSTER: Local orbital projections, atomic charges, and chemical-bonding analysis from projector-augmented-wave-based density-functional theory, *J. Comput. Chem.*, 2020, **41**, 1931–1940.
32 S. Maintz, V. L. Deringer, A. L. Tchougréeff and R. Dronskowski, LOBSTER: A tool to extract chemical bonding from plane-wave based DFT, *J. Comput. Chem.*, 2016, **37**, 1030–1035.
33 J. K. Nørskov, T. Bligaard, A. Logadottir, J. R. Kitchin, J. G. Chen, S. Pandelov and U. Stimming, Trends in the exchange current for hydrogen evolution, *J. Electrochem. Soc.*, 2005, **152**, J23.
34 B. Hinnemann, P. G. Moses, J. Bonde, K. P. Jørgensen, J. H. Nielsen, S. Horch, I. Chorkendorff and J. K. Nørskov, Biomimetic hydrogen evolution: MoS_2 nanoparticles as catalyst for hydrogen evolution, *J. Am. Chem. Soc.*, 2005, **127**, 5308–5309.
35 V. Wang, N. Xu, J.-C. Liu, G. Tang and W.-T. Geng, VASPKIT: A user-friendly interface facilitating high-throughput computing and analysis using VASP code, *Comput. Phys. Commun.*, 2021, **267**, 108033.
36 M. Naguib, V. N. Mochalin, M. W. Barsoum and Y. Gogotsi, 25th anniversary article: MXenes: a new family of two-dimensional materials, *Adv. Mater.*, 2014, **26**, 992–1005.
37 M. Dahlqvist and J. Rosen, Predictive theoretical screening of phase stability for chemical order and disorder in quaternary 312 and 413 MAX phases, *Nanoscale*, 2020, **12**, 785–794.
38 H. Liu, X. Jia, A. Cao, L. Wei, C. D'agostino and H. Li, The surface states of transition metal X-ides under electrocatalytic conditions, *J. Chem. Phys.*, 2023, **158**, 124705.
39 W. Yang, Z. Jia, B. Zhou, L. Wei, Z. Gao and H. Li, Surface states of dual-atom catalysts should be considered for analysis of electrocatalytic activity, *Commun. Chem.*, 2023, **6**, 6.
40 Z. Guo, T. Wang, J. Xu, A. Cao and H. Li, Surface coverage and reconstruction analyses bridge the correlation between structure and activity for electrocatalysis, *Chem. Commun.*, 2024, **60**, 14346–14359.
41 H. Liu, D. Zhang, S. M. Holmes, C. D'Agostino and H. Li, Origin of the superior oxygen reduction activity of zirconium nitride in alkaline media, *Chem. Sci.*, 2023, **14**, 9000–9009.

42 J. Zhang, Y. Zhao, X. Guo, C. Chen, C.-L. Dong, R.-S. Liu, C.-P. Han, Y. Li, Y. Gogotsi and G. Wang, Single platinum atoms immobilized on an MXene as an efficient catalyst for the hydrogen evolution reaction, *Nat. Catal.*, 2018, **1**, 985–992.

43 G. Gao, A. P. O'Mullane and A. Du, 2D MXenes: A new family of promising catalysts for the hydrogen evolution reaction, *ACS Catal.*, 2017, **7**, 494–500.

44 B. C. Wyatt, A. Thakur, K. Nykiel, Z. D. Hood, S. P. Adhikari, K. K. Pulley, W. J. Highland, A. Strachan and B. Anasori, Design of atomic ordering in $Mo_2Nb_2C_3T_x$ MXenes for hydrogen evolution electrocatalysis, *Nano Lett.*, 2023, **23**, 931–938.

45 S. Trasatti, Electronegativity, work function, and heat of adsorption of hydrogen on metals, *J. Chem. Soc., Faraday Trans.*, 1972, **1**(68), 229–236.

46 A. L. Allred, Electronegativity values from thermochemical data, *J. Inorg. Nucl. Chem.*, 1961, **17**, 215–221.

47 Y. Gogotsi and B. Anasori, The Rise of MXenes, *ACS Nano*, 2019, **13**, 8491–8494.

48 H. Kwon, J. Park, J. E. Shin and B. Koo, Optimal investment strategy analysis of on-site hydrogen production based on the hydrogen demand prediction using machine learning, *Int. J. Energy Res.*, 2024, **17**, 6313421.

49 M. V. Jyothirmai, R. Dantuluri, P. Sinha, B. M. Abraham and J. K. Singh, Machine-learning-driven high-throughput screening of transition-metal atom intercalated g-C_3N_4/MX_2 (M = Mo, W; X = S, Se, Te) heterostructures for the hydrogen evolution reaction, *ACS Appl. Mater. Interfaces*, 2024, **2024**, 12437–12445.

50 S. Ringe, N. G. Hörmann, H. Oberhofer and K. Reuter, Implicit solvation methods for catalysis at electrified interfaces, *Chem. Rev.*, 2022, **122**, 10777–10820.